Evaluation of sensors for the detection of energy resolved very soft x-ray fluorescence

Conference or Workshop Item

Evaluation of sensors for the detection of energy resolved very soft x-ray fluorescence

Lawrence Jones, Chiaki Crews, Matthew Soman, James Ivory, Andrew Holland

Lawrence S. Jones, Chiaki Crews, Matthew Soman, James Ivory, Andrew D. Holland, "Evaluation of sensors for the detection of energy resolved very soft x-ray fluorescence," Proc. SPIE 12191, X-Ray, Optical, and Infrared Detectors for Astronomy X, 1219118 (29 August 2022); doi: 10.1117/12.2629344

SPIE.

Event: SPIE Astronomical Telescopes + Instrumentation, 2022, Montréal, Québec, Canada

Evaluation of sensors for the detection of energy resolved very soft X-ray fluorescence

Lawrence S. Jones*[a], Chiaki Crews [a], Matthew Soman[a], James Ivory[a], Andrew D. Holland[a]
[a]Centre for Electronic Imaging (CEI), the Open University, Milton Keynes, UK

ABSTRACT

Energy-dispersive imaging spectroscopy of X-ray emission from the Earth's aurorae promises to further knowledge in the field of aeronomy. Time- and spatially-resolved observations of fluorescence from the dominant atmospheric components require the detection of X-rays as soft as 390 eV with a resolution of no more than 100 eV at these energies. The Auroral X-ray Imaging Spectrometer (AXIS) instrument of the Disturbed and quiet time Ionosphere-thermosphere System at High Altitudes (DISHA) mission is expected to perform these observations.

The baseline instrument design has suggested the use of an electron-multiplying charge-coupled device (EMCCD). The EMCCD's electron-multiplying register can reduce the effective readout noise and enable the detection of signals as small as a single photoelectron. For the detection of soft X-rays, however, the noise penalty from the EM register's stochastic process degrades energy resolution.

Emerging CMOS image sensors (CIS), particularly the Teledyne e2v CIS221-X test device, with back illumination, full depletion (with 36 µm thickness), large pixel sizes (40 µm), and low readout noise (3 e- rms effective) are expected to achieve the required performance without the effects of the EM register. Simple models for X-ray event sensitivity, detectability, and resolution, indicate that candidate CIS equal or better EMCCD performance. Furthermore, CIS offer other advantages including lower power consumption, higher operating temperature, and increased radiation hardness. However, these sensors introduce other behaviors that may impact their apparent benefits, which initial experimental testing and analyses are working to understand.

Keywords: CCD, EMCCD, CIS, Soft X-ray, AXIS, DISHA, imaging spectroscopy

1. INTRODUCTION

The Disturbed and quiet-type Ionosphere System at High Altitudes (DISHA) mission by the Indian Space Research Organization (ISRO) is a twin satellite mission planned to be launched into polar orbit to study the aeronomy of Earth, investigating the interactions of the uppermost layers of the atmosphere with the environment of space. DISHA completed a successful Baseline Design Review (BDR) in 2020, which included the Auroral X-ray Imaging Spectrometer (AXIS) instrument on the DISHA-H satellite. AXIS is intended to observe X-ray emission from the upper layers of the Earth's atmosphere using a wide field of view (FOV) camera. On DISHA-H, AXIS's main goal and normal mode of operation will be to collect X-ray fluorescence emission maps for very soft X-ray energies (300 eV to 2000 eV) at a spatial resolution of a few tens of km for the first time. A second mode of operation is also proposed where the pointing of the camera is adjusted to observe Solar Wind Charge Exchange (SWCX), another source of X-ray emission generated via the excitation of atmospheric ions by the solar wind.

These science goals generate an interesting challenge from the perspective of the X-ray detector, as the required spectral resolution results in the need for one able to accurately measure signals of around 100 e^- and gather this charge from X-rays with attenuation lengths of less than a micron. With effective readout noise values of <1 e^-, electron-multiplying charge-coupled devices (EMCCDs) would appear to be an ideal candidate, however the electron multiplying mechanism has its own drawbacks. Alternatively, CMOS image sensors (CIS) are approaching levels of performance that would be sufficient for AXIS but without requiring the electron multiplication process and offering other secondary benefits such as increased radiation tolerance.

X-Ray, Optical, and Infrared Detectors for Astronomy X, edited by Andrew D. Holland, James Beletic
Proc. of SPIE Vol. 12191, 1219118 · © 2022 SPIE · 0277-786X · doi: 10.1117/12.2629344

This paper presents a trade-off study of the candidate X-ray detectors for AXIS, including a review of the sensors and their interaction with mission requirements, and a side-by-side experimental performance comparison for soft X-ray detection in the 390 eV to 2000 eV range.

1.1 Mission requirements

To achieve the science aims of the AXIS instrument, to observe both atmospheric X-ray fluorescence and electron bremsstrahlung, the X-ray detector is required to be sensitive to X-rays from 300 eV to 2000 eV. In addition, to separate the effects of the critical fluorescence lines and accurately measure the bremsstrahlung shape, the X-ray detector must have an energy resolution <100 eV at 500 eV. Alongside these energy resolution requirements there are spatial resolution requirements placed on the detector to enable the resolution of auroral structures. However, the spatial requirements are not as demanding and all X-ray detectors considered met them, therefore consideration of spatial performance is beyond the scope of this paper.

The baseline instrument design uses a CCD201-20 operating in photon counting mode in which the charge from each X-ray can be resolved into individual interaction events (illustrated in Figure 1). To screen unwanted optical and UV light, a 120 nm-thick aluminum optical blocking filter will be applied directly to the X-ray detector. A pinhole camera will be used to provide spatial resolution, with a 5 km × 5 km footprint for each pixel over a 110° field of view if using this baselined detector. This configuration is expected to result in an X-ray count rate of 8 counts/s when viewing the aurora during periods of low activity, and 0.04 counts/s when viewing regions of SWCX [1].

Table 1. Summary of baseline design instrument parameters.

Parameter	Value
X-ray detector	CCD201-20
Optical blocking filter	Directly deposited 120 nm Al
Expected count rate	8 counts/s (aurora) 0.04 counts/s (SWCX)

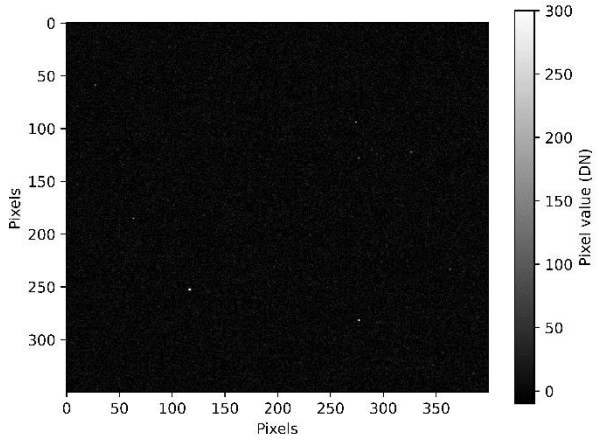

Figure 1. Readout extract from CCD201-20 showing resolved X-rays as scattered spotting in the image.

1.2 Sensor candidates

Starting with the baselined CCD201-20, a range of X-ray detectors have been identified for evaluation based on the potential performance benefits that they can provide for AXIS. This includes the CCD201-20 derived CCD311, and CIS that potentially meet performance requirements: the CAPELLA 45 and CIS221-X.

The CCD201-20 is an EMCCD, utilizing an electron multiplying (EM) register prior to readout to generate high gain and suppress the noise contribution of the readout amplifier. This enables detectors of this type to detect pixel signals as small as a single electron, and easily identify X-ray charge packets from the lower end of the required sensitivity. The CCD201-

20 has been the subject of detailed study in relation to the Coronagraph Instrument (CGI) aboard NASA's Nancy Grace Roman Space Telescope (NGRST). This means that there is a developed understanding of its performance after irradiation, and the technology readiness level (TRL) of the sensor has been raised [2]. The CCD201-20 is an ideal sensor for schedule and cost requirements as it is already commercially available.

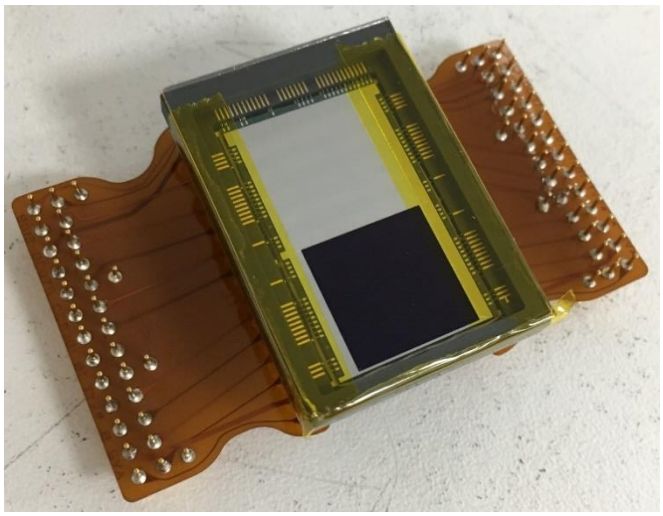

Figure 2. CCD201-20 used in this investigation, mounted on electrical interface flexi circuits. The protective glass cover is used to prevent the sensor being damaged during handling and is removed before tests.

CGI work for the CCD201-20 has led to the development of the CCD311, which includes modifications to the CCD201-20 design to improve radiation hardness. These include narrowed charge collection channels to reduce charge transfer inefficiency (CTI) susceptibility and overspill drains to protect the gain register [3]. These sensors are under development specifically for NGRST, therefore there are some concerns about their availability. For the purposes of this study its unirradiated performance is expected to be equivalent to the CCD201-20.

A drawback of EMCCDs for the purposes of the AXIS instrument is the additional X-ray energy uncertainty generated by the stochastic processes of the EM register [4]. When operating at the gain levels required to achieve the desired sensitivity, the resulting signal-dependent X-ray event signal variance can increase by a factor of ten. Alternative X-ray detectors with a noise floor low enough to enable detection of the softest X-rays, but without the penalty of the EM register, offer the potential for increased energy resolution. Developments in CIS technology indicate that their soft X-ray imaging spectroscopy performance may now be comparable to CCDs and EMCCDs, with potential advantages for AXIS. They use the active pixel sensor (APS) architecture with charge to voltage readout circuits in each pixel, resulting in increased readout speed and radiation tolerance. This should permit the candidate CIS X-ray detectors to operate at higher temperatures and for a longer mission duration. Furthermore, CIS generally have lower overall power and complexity requirements due to the elimination of the EM register and its high voltage clock phase.

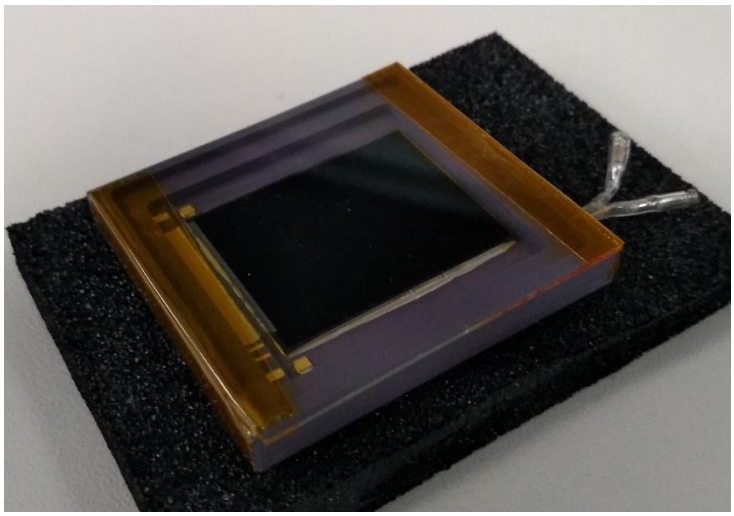

Figure 3. CAPELLA 45 sensor used in this investigation. The uniform surface color indicates that this is a backside illuminated (BSI) sensor.

The CAPELLA 45 CIS manufactured by Teledyne e2v [5] is intended as a general-purpose sensor. It features a 20 mm × 20 mm pixel area with 10 µm square pixels and a full well depth of 39,000 e^-, using architectures inherited from the Sirius CIS115 due to fly aboard JUICE's JANUS camera [6]. The CAPELLA sensors integrate many additional on-chip functions including readout and pixel driving. Most interactions with the chip including setup, frame grabbing, and data transfer occur over digital interfaces. This is expected to have additional benefits due to less complex supporting electronics requirements. The CAPELLA 45 has been included in this study as a CIS of moderate heritage. While it is not expected to be the most suitable CIS under test it will be used to further investigate CIS behaviors. Additionally, the CAPELLA 45 represents a "halfway" sensor between the CCD201-20 and the CIS221-X. The CAPELLA 45 used was back illuminated, only partially depleted, and had pixel sizes with 10 µm pitch, like the CCD201-20, but as a CIS it exhibits many of the per pixel variation behaviors that will need to be accounted for in the CIS221-X.

The CIS221-X is a test sensor resulting from development of the CAPELLA 45 architecture to improve soft X-ray performance [7]. It includes deep depletion extension implants to permit deep depletion of the device substrate; three pixel variants of increased pixel size (40 µm square) to reduce X-ray event charge sharing; reduced readout noise and increased charge to voltage factor to improve performance at lower X-ray energies; and additional pinning implants to reduce the charge storage volume within each pixel and reduce image lag. The CIS221-X is expected to demonstrate key technologies and design features that will enable the development of future scientific CIS X-ray detectors. Initial testing of the CIS221-X has demonstrated near Fano-limited energy resolution [8].

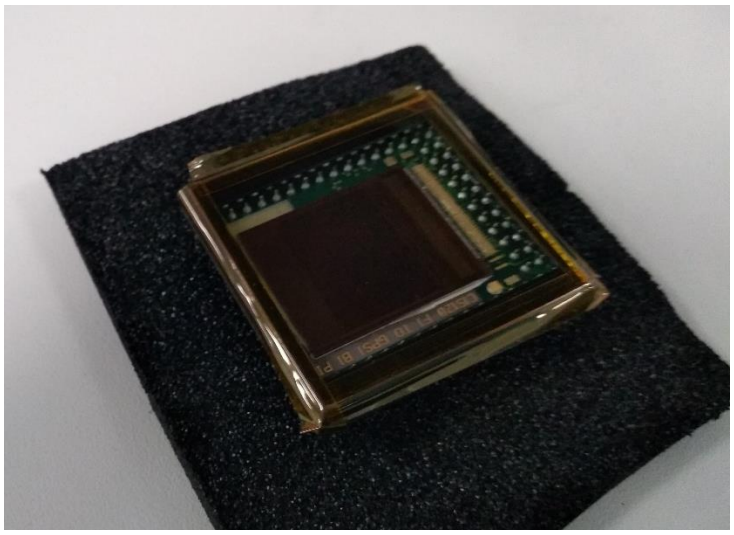

Figure 4. CIS221-X sensor used in this investigation, mounted in an interim PCB package. Only a frontside illuminated (FSI) device was available at the time of this study, in which X-rays must first traverse the detector control structures to reach the X-ray sensitive silicon.

Finally, the CCD370 has been included for initial theoretical comparisons between the candidate X-ray detectors and the current state of the art X-ray optimized CCDs to demonstrate the advantage of the alternate architectures. The CCD370 is a large area X-ray optimized CCD, designed for use in the Solar wind Magnetosphere Ionosphere Link Explorer (SMILE) Soft X-ray Imager (SXI) [9]. Compared to a standard CCD, these X-ray detectors have an increased charge to voltage factor, enhanced back-surface passivation, and are intended to be used in a 6×6 pixel binning mode, resulting in an effective pixel size of 108 µm × 108 µm. Charge transfer inefficiency (CTI) is a particular concern for the CCD370 due to its large photosensitive area (8 cm × 8 cm), so many of the mitigation measures included in the CCD311 are also used in the CCD370. This sensor is a useful benchmark for evaluating the performance of the EMCCD and CIS alternatives, however it is immediately disqualified from consideration as it will not be available in the time frame required for AXIS.

Table 2. Summary of devices included in this study.

	CCD201-20	**CCD311**	**CAPELLA 45**	**CIS221-X**	**CCD370**
Technology	EMCCD	EMCCD	CIS	CIS	CCD
Pixel pitch (µm)	13	13	10	40	108*
Thickness (µm)	16	16	16	35	16
Readout noise (e^-)	(EM register)	(EM register)	6	3	5.3
Radiation hardness	Low	Moderate	High	High	Moderate
Technology readiness	Moderate	Moderate	Low	Low	Moderate
Availability	Commercial	Unknown	High	Low	No

*With on-chip binning.

2. MODELLED PERFORMANCE

Understanding the differences between the candidate X-ray detectors began with an extrapolation of each detector's properties into key performance characteristics. The three key performance metrics that were explored in this way were: sensitivity (the ability of each sensor to collect the charge resulting from X-rays); detectability (the expected yield of X-

ray events compared to the total number of events absorbed); and energy resolution (the X-ray fluorescence peak FWHM that may be expected from each detector).

2.1 Sensitivity

The sensitivity of the candidate X-ray detectors was predicted using a layer-cake model, previously used during measurements of soft X-ray quantum efficiency (QE) in a CCD97, another EMCCD [10]. All devices are modelled as backside illuminated (BSI), with an enhanced back surface passivation used to reduce the non-sensitive back surface layer, and including the optical blocking filter planned for AXIS, with the resulting QE predictions plotted in Figure 5. This method does not take horizontal structures into account, therefore because the strata of all the candidate X-ray detectors other than the CIS221-X are very similar, they may be represented with the same layer cake model.

The layer-cake method was extended to predict the proportion of X-rays expected to be absorbed in the field-free region of the partially depleted devices (CCD201-20, CAPELLA 45, CCD370) by plotting two traces for these devices: including and excluding the field-free region. When the QE including this region is significantly higher than the QE excluding this region, we may expect many X-rays to be absorbed in the field-free region where they are likely to spread their charge over many pixels before being collected.

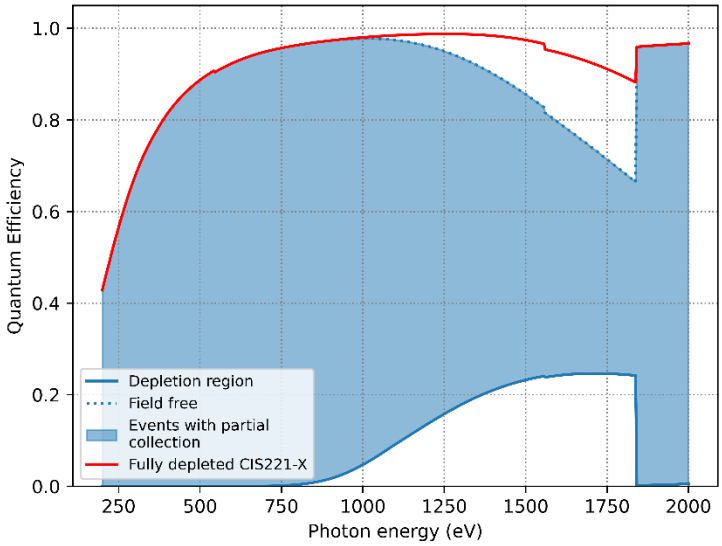

Figure 5. X-ray quantum efficiency predictions from 250 eV to 2000 eV.

This model indicated that all candidate X-ray detectors should have sufficient sensitivity (>0.7 QE) over the required energy range. Below 1 keV the populations of X-rays in the partially depleted devices are very likely to be dominated by split events. This has implications for detectability, as split events will be harder to detect because less charge will be collected in any single pixel, and for spectral resolution, as events spread over multiple pixels will be more affected by per-pixel noise sources.

2.2 Detectability

Another key performance attribute is the detectability of X-rays in each sensor. Assuming complete charge collection, this is the probability that the charge of an X-ray event (γ_{sig}) added to the noise of the detector (σ_{pix}) will exceed a detection threshold (γ_{thresh}), and can be expressed as equation 1:

$$P_{detect} = P\left((\gamma_{sig} + \sigma_{pix}) > \gamma_{thresh}\right) \quad (1)$$

Because the charge of X-ray events increases with X-ray energy, this is primarily an issue at the lower end of the energy range of interest. The probability of X-ray detection will further reduce the sensitivity of each X-ray detector, as X-rays successfully absorbed but then discarded as noise do not contribute to science. If we assume that the noise of the device is largely Gaussian, we may express the detection probability as per equation 2 (and presented in Figure 6):

$$P_{detect} = \frac{1}{2}\left(1 - \mathrm{erf}\left(\frac{\gamma_{\mathrm{thresh}} - \gamma_{\mathrm{pix}}}{\sigma_{pix}\sqrt{2}}\right)\right) \quad (2)$$

The X-ray event threshold for a particular detector is often a multiple of the per pixel rms noise above the zero value (for example, [11]). This is selected to ensure maximum detectability of X-rays whilst suppressing the number of noisy pixels falsely identified as X-rays. For the following predictions a detection threshold of 5 times the rms noise value has been used, to reflect the harsh event identification criteria that will be required to prevent the low-flux low-energy X-rays expected to be observed by AXIS from becoming lost among mis-identified noisy pixels.

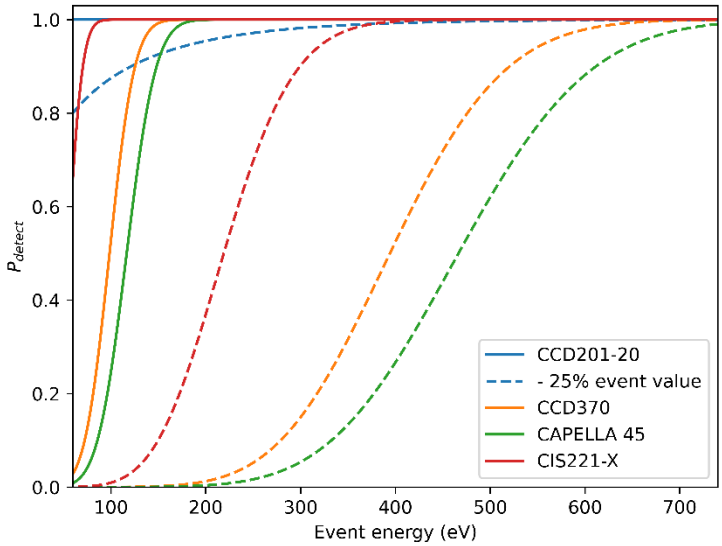

Figure 6. Event detection probability for energy in the four modelled devices.

This highlights a large advantage of the EMCCDs, because readout noise is suppressed, per-pixel variations are low, and X-ray charge is straightforward to separate from any noise background, even for very low X-ray energies. Figure 6 indicates that a CCD201-20 will be able to identify X-ray signals down to signals <10 e^-. This means that even X-ray charge clouds split across multiple pixels will be identifiable, indicated by the detection probability for 25% of the event value. On the other hand, because of their unsuppressed readout noise, the CCD370 and CIS show far worse performance. While all three are predicted to be able to detect single pixel events, the CCD370 and CAPELLA 45 show a low detection probability for split events from X-rays of energies that extend into the range of interest.

Alternatively, we may use equation 2 to predict event detection probability at a fixed energy but with increasing noise provided by some extra noise source, shown in Figure 7 for 390 eV.

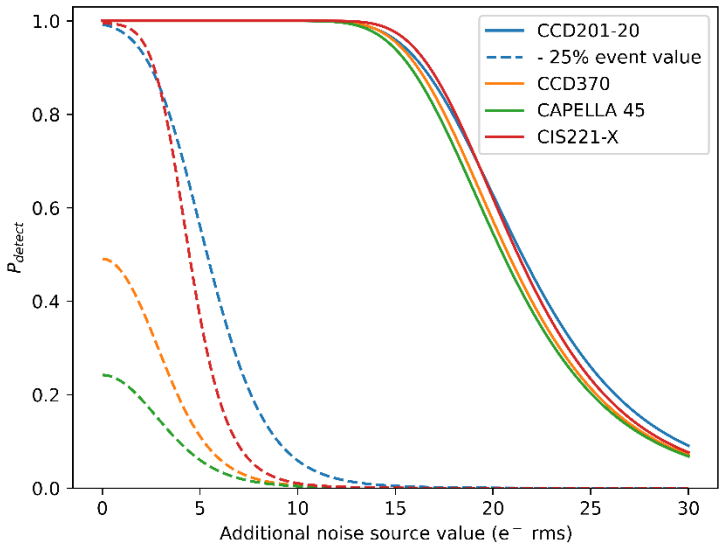

Figure 7. X-ray detection probability for a fixed energy, 390 eV (nitrogen Kα), with increasing noise provided by an additional noise source.

The split event 25% trace shows a difference between the X-ray detectors. The CCD370 and CAPELLA 45 are not suitable for split event detection at this energy. The CIS221-X and the CCD201 quickly become unusable for detecting split events in the presence of external noise, indicating that these devices have an excess noise budget of around 5 e^-. However, this analysis has effectively modelled additional noise within each pixel, when in practice any noise external to the EMCCD due to additional electronics or quantization will be suppressed by the EM register.

2.3 Spectral Resolution

Achieving the required spectral resolution of AXIS, here defined with peak FWHM, will be critical for enabling in-depth analysis of data and distinguishing atmospheric component fluorescence from the electron bremsstrahlung. The total uncertainty (noise) in the measurement of any given X-ray is modelled by equation 3, which represents a best-case scenario:

$$\sigma_{X-ray,e^-} = \sqrt{\frac{F.\,\mathrm{E_{X-ray}}}{3.65} + \sigma^2_{readout}} \tag{3}$$

Where F is the Fano factor (0.115 in silicon, 1.115 for an EMCCD including the EM register excess noise [12]), E_{X-ray} is the X-ray energy in eV, and $\sigma^2_{readout}$ is the readout noise of the device. It has been assumed that in the final instrument design the operating temperature will be selected to ensure negligible dark current, and this method does not capture more complex sources of uncertainty including event reconstruction and CTI. X-ray uncertainty can be converted into spectral resolution using equation 4:

$$FWHM_{eV} = 2.355\,.\,3.65\,.\,\sigma_{X-ray,e^-} \tag{4}$$

Which is a conversion of noise in electrons rms to eV FWHM. Using the noise values for each X-ray detector, the predicted FWHM of X-ray event peaks within each was calculated and plotted in Figure 8.

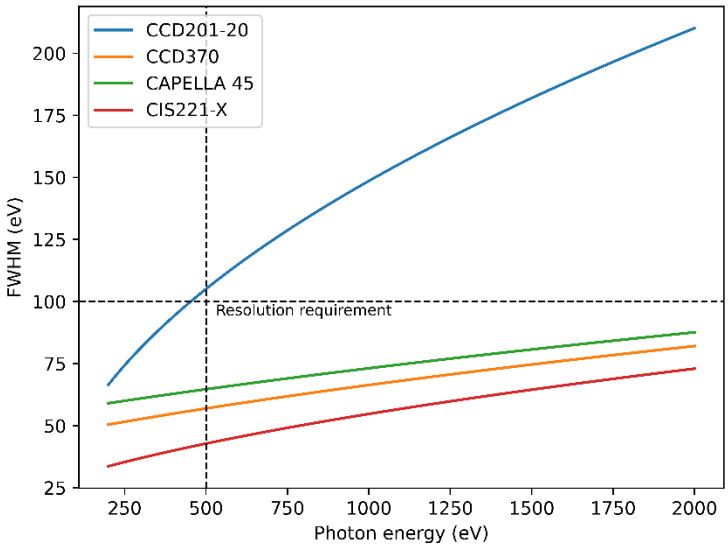

Figure 8. Spectral resolution predictions for all X-ray detectors, expressed as FWHM.

This indicates that if noise were restricted to those sources included in the model, all the alternative X-ray detectors under consideration would achieve the required spectral performance. The effect of the EM register on the spectral resolution of the CCD201-20 (as discussed in section 1.2) results in it not meeting the 500 eV energy resolution requirement. The CCD201-20 is not discounted at this point, however, as its expected performance is only slightly worse than required, and it shows far better detectability properties than the other candidate detectors, as well as their other advantages.

Like the method used for detectability in Figure 7, we may instead resolve equation 3 while varying the noise parameter, rather than energy, as shown in Figure 9. The resolution of the CIS and CCD370 are only degraded beyond the required resolution with an additional noise source of > 8 e^- rms, indicating that detectability is the limiting performance parameter in these X-ray detectors, rather than resolution. The CCD201-20 begins with marginal energy resolution requirement compliance and so has a noise budget of 0 e- rms, though as the noise source modelled in this plot has not been suppressed by the EM register (that is, it is modelled as occurring within each pixel), off-chip noise can largely be ignored, even for significant increases.

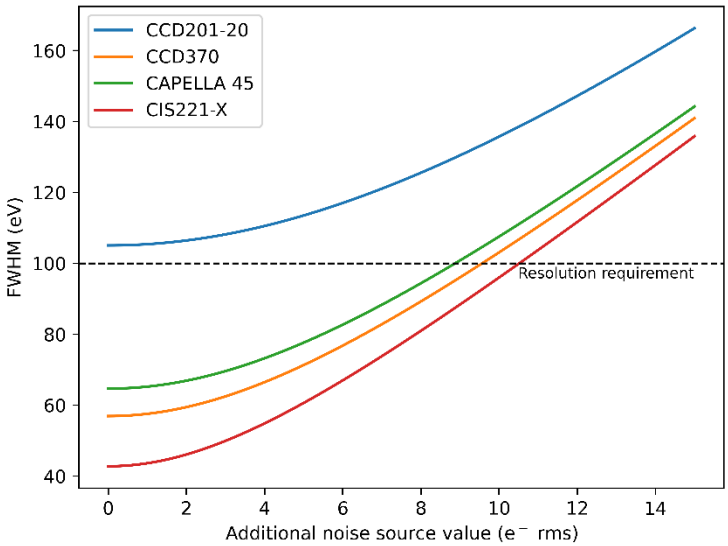

Figure 9. X-ray energy resolution probability for a fixed energy, 500 eV, with increasing noise provided by an additional noise source.

3. PRACTICAL DEMONSTRATION OF X-RAY DETECTORS

Practical demonstrations of the candidate X-ray detectors were performed with X-rays within the required energy range. Results were used to measure X-ray uncertainty, in particular the excess of this value above ideal Fano-limited performance. All detectors were tested by exposure to soft X-rays from a selection of fluorescence targets, though for brevity only the results from a single target have been explored below for each.

3.1 Experimental Setup

To test the candidate X-ray detectors, the apparatus illustrated in Figure 10 was assembled to operate the detectors under vacuum at representative temperatures whilst exposed to soft X-ray radiation.

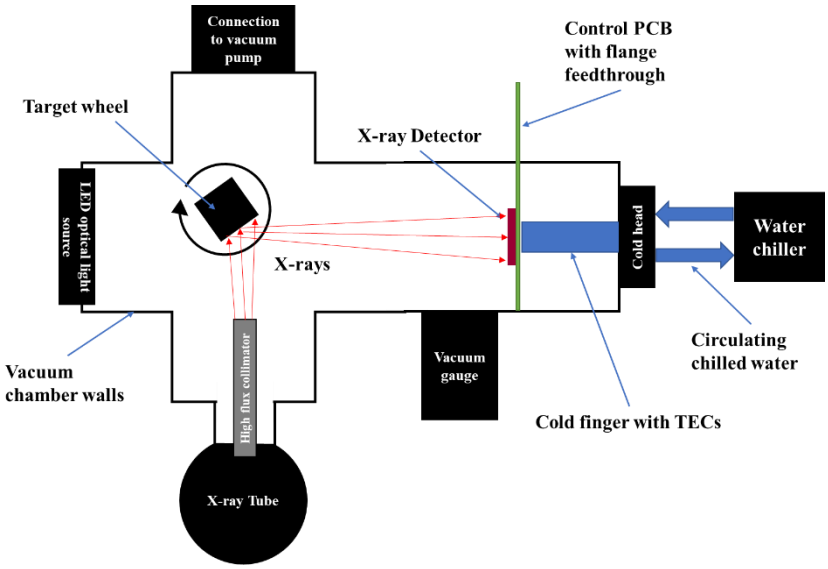

Figure 10. Top-down schematic view of X-ray detector test apparatus. CIS mounting shown; there were slight differences for the CCD201-20.

Soft X-rays were generated with an X-ray tube and fluorescence targets of known chemical compositions. Cooling for all X-ray detectors was achieved with water-cooled thermo-electric coolers (TECs) under closed loop control. This enabled X-ray detector temperatures of less than -30 °C, which was sufficient to suppress dark current generation.

3.2 CCD201-20

The CCD201-20 was not tested in the standard chamber due to flange compatibility issues, however the only differences were a slightly longer throw between the fluorescence target and sensor and a calibration iron-55 source placed in the sensor field of view producing a steady flux of Mn Kα and Mn Kβ X-rays. A typical spectrum of X-ray event energies observed with this device is shown in Figure 11 (with an MgF_2 target).

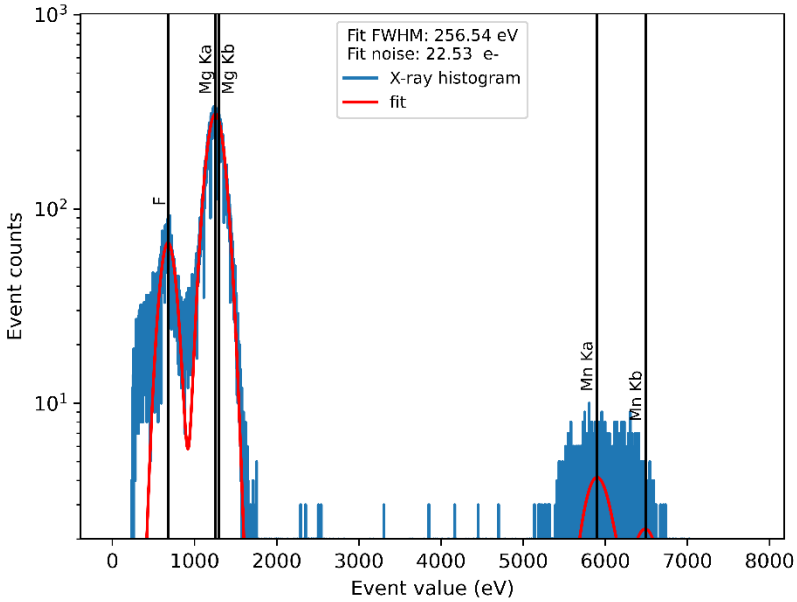

Figure 11. Typical X-ray fluorescence spectrum observed with CCD201 using an MgF_2 target; fit based on Mg Kα peak at 1254 eV. Fluorine Kα (677 eV) fluorescence is clearly distinguishable.

The FWHM observed when measuring the spectrum of energies from all detected events was consistent with an additional noise source in the detector and event reconstruction process equal to around 22 e^- rms, approximately uniform for energy. FWHM, and measured noise, could be reduced by down selecting the detected events, though this comes at the cost of event yield. For instance, restricting event selection to single pixel events quickly reduces the FWHM to the theoretical limit but excludes 80% to 100% of events. The reason for this is shown in Figure 12, the 'mean X-ray' of all the Al Kα X-rays detected, which indicates that for the average X-ray a considerable portion of the total X-ray generated charge collected is gathered in pixels other than the one in which the X-ray was initially incident. This spreading is primarily caused by the diffusion of charge in the field free region close to the back surface of the X-ray detector.

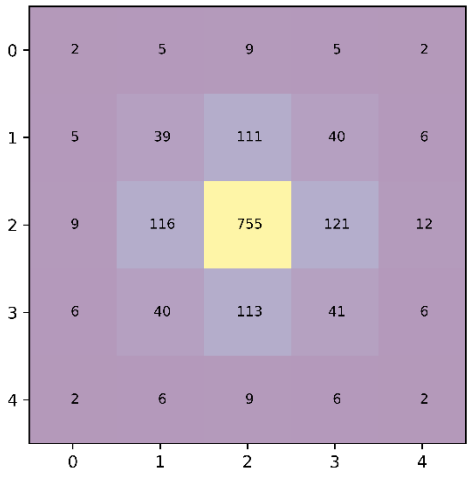

Figure 12. Mean value of pixels for all aluminum Kα X-rays (1490 eV) detected in the CCD201. Pixel values are in eV.

An issue for the candidate EMCCD X-ray detectors is the effect of CTI, as can be seen in Figure 12: pixel values surrounding the central, incident, pixel have a clear bias to the bottom right, which corresponds to the readout direction (up then left).

Additionally, in spectra formed from all detected X-rays, significant peak 'shoulders' were observed on the lower energy sides of lower energy fluorescence peaks. This is thought to be due to event reconstruction excluding pixels containing small numbers of X-ray generated electrons but falling below the threshold level used. This will be a particular issue at lower energies when the X-rays are more likely to interact in the field free region far from the charge collection channel.

Overall, the CCD201-20 displayed performance sufficient for AXIS, including demonstrating sub-1 keV X-ray detection capability and near ideal energy resolution, following event down selection. Further work on event detection and operation optimization in this device may enable more accurate reconstruction and detection of events or lower the event yield penalty for down selecting detected X-rays to improve performance.

3.3 CAPELLA 45

The energy resolution performance of the CAPELLA 45 was best measured with X-rays fluoresced from the copper fluorescence target (shown in Figure 13). Stray X-rays, both from the X-ray tube and from the fluoresced target, produced further fluorescence lines from other chamber elements, ranging from 4500 eV to 7000 eV. Fitting to the spectrum observed indicated that the device was operating with an extra 59 e^- (rms) of noise, which was not reduced satisfactorily by applying selection criteria to the detected X-rays.

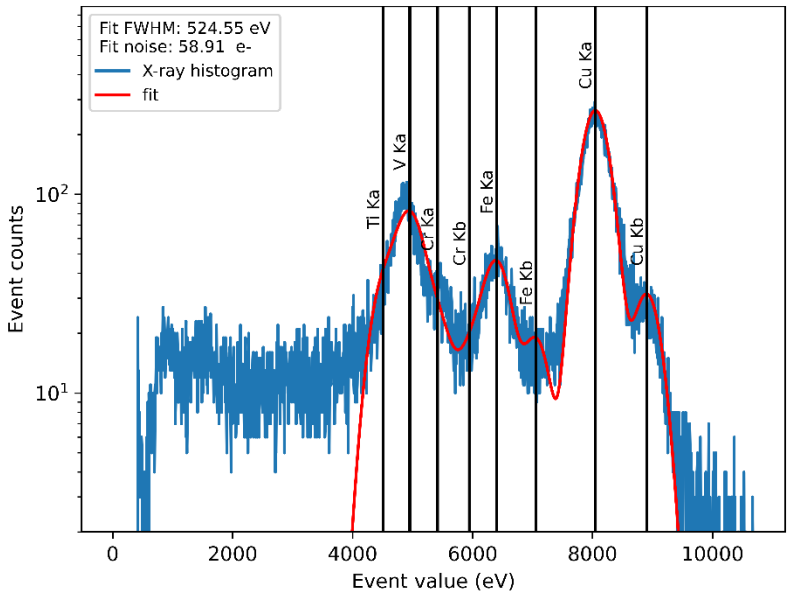

Figure 13. Spectrum from CAPELLA 45 using a Cu fluorescence target fluorescence from the test chamber is also observed.

The mean X-ray observed in the CAPELLA 45 (Figure 14) showed similar event spreading to the CCD201-20, indicating that on average the charge generated by incoming X-rays was spread over many pixels. This means that the 25 % traces of Figure 6 and Figure 7 are appropriate for assessing the likely performance of this detector. Reassuringly, the mean image does not show the skew indicative of CTI.

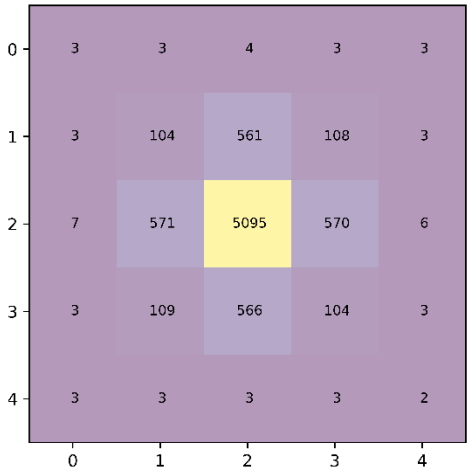

Figure 14. Mean value of pixels for all copper Kα X-rays (8042 eV) detected in the CAPELLA 45. Pixel values are in eV.

The performance of the CAPELLA 45 studied was not sufficient for AXIS. Background noise was sufficient to obscure the signal from most X-rays below 1 keV, as the per pixel noise in this particular device exceeded datasheet values. The charge from X-ray events was regularly split over many pixels (as shown in Figure *14*), in a manner similar to the CCD201-20, resulting in the high additional noise from event reconstruction seen when fitting to the fluorescence spectra. The presence of a large field free region at the back surface of the device enables X-ray generated charge to spread across many pixels, compounding issues associated with the large per-pixel noise in this device. Spectral resolution was therefore insufficient to resolve energies of <2 keV X-rays.

3.4 CIS221-X

The CIS221-X performed well, matching expectations, and displaying noise consistent with energy resolution requirements. Because the X-ray detector tested was front illuminated, its sensitivity to <1 keV electrons was limited, and testing was conducted with an Al fluorescence target. The population of X-rays observed was dominated by interactions within a single pixel. Fitting to the resulting spectra indicated that the total additional noise due to the X-ray detector was 8 e^- rms and therefore within the margin for the device to achieve the energy resolution performance required by AXIS. All analyses of the CIS221-X used the 40 µm third variant pixels, which have been shown to have the best performance of the three 40 µm variants in previous testing [8].

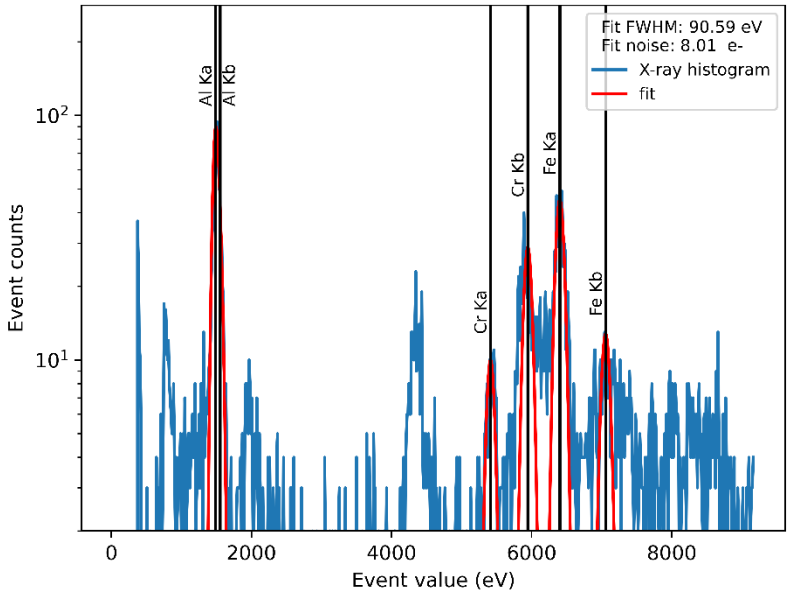

Figure 15. Typical X-ray fluorescence spectrum observed with CIS221-X using an aluminum target; fit based on Al Kα peak at 1487 eV and secondary fluorescence peaks generated by the test chamber.

The dominance of single pixel events is seen in the 'mean event' for the aluminum peak. No event down-selection has been conducted, and yet the energy collected is clearly dominated by the central pixel, and negligible energy was collected from pixels in the outer 5x5 ring. This demonstrates the benefits of fully depleting the sensor, and of the 40 µm pixels.

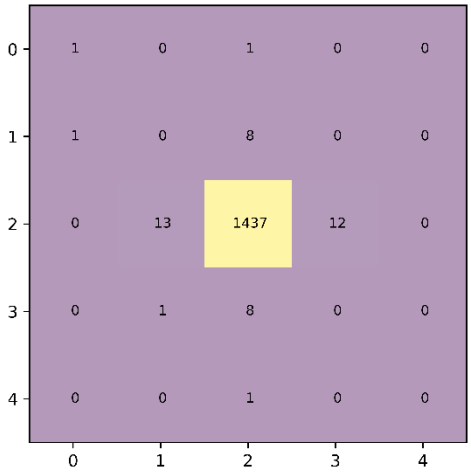

Figure 16. Mean value of pixels for all aluminum Kα X-rays (1490 eV) detected in the CIS221-X. Pixel values are in eV.

While <1 keV X-rays could not be observed, this testing did permit the observation of the X-ray detector noise floor. The noise floor represents a minimum energy below which any real X-rays identified are significantly outnumbered by misidentified noisy pixels. This is shown in Figure 17, which compares the spectrum of X-ray events identified to a corresponding spectrum of background pixels, collected with the X-ray tube turned off. This plot demonstrates that the large increase in events incorrectly identified at low energy correspond to the larger numbers of pixels that have equivalent values due to noise. This indicates that the lowest X-ray energy that could confidently be identified in the CIS221-X is around 350 eV, however many of the background events above 200 eV are due to consistently noisy or hot pixels which are an ongoing area of investigation in CIS development. The energy of the noise floor cutoff is expected to be reduced as

understanding of the CIS221-X increases, and the corresponding improvement in X-ray identification and noise rejection techniques.

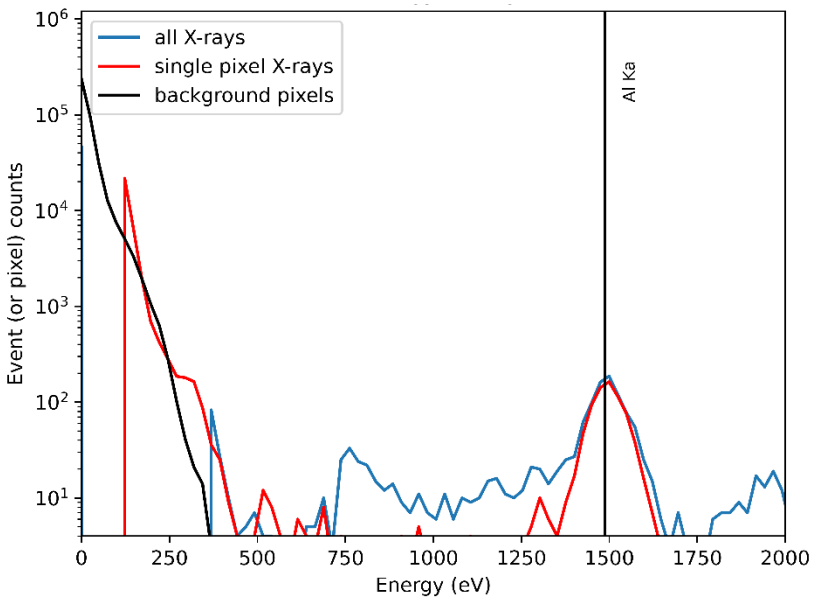

Figure 17. Comparison of energy spectra at <2 keV. The 'all X-ray' detection threshold is considerably higher than the single pixel threshold, due to the factors discussed in section 2.2.

This is a good indication that the CIS221-X is capable of the performance required by AXIS, however crucial behaviors have not yet been tested. The performance of the X-ray detector below 1 keV has not been explored because of the large attenuation of these X-rays in the dead layers of the front surface of this front-illuminated test device. The observed noise floor, while a positive sign, is not truly representative of final performance as in a back illuminated X-ray detector, as X-rays of energies close to the observed noise floor would exhibit other behaviors including charge spreading near the back surface, which will be investigated in the near future. An additional factor in the acceptance of the CIS221-X, its performance after irradiation, will also be tested and reported in future publications. The performance seen, however, leaves considerable margin for radiation-induced degradations in energy resolution and sensitivity.

4. DISCUSSION AND CONCLUSIONS

The CCD201-20, unirradiated, appears to operate in a manner consistent with the requirements for AXIS. However, performance degradation due to irradiation during flight may prove problematic. Additional sources of X-ray energy uncertainty including CTI (seen in the unirradiated device) and dark current may quickly reduce the ability of the EMCCD to perform well enough below 1 keV. The CCD311 offers increased resilience to radiation damage which may mitigate these effects. These X-ray detectors have demonstrated the ability to approach their theoretical energy resolution limits, and further optimizations may permit these limits to be reached without corresponding losses to X-ray detectability.

The CAPELLA 45 did not demonstrate behaviour consistent with the requirements of AXIS, despite favorable results in initial modelling. The CAPELLA 45 is unlikely to be suitable for AXIS and unfortunately showed noise high enough that it obscured many of the CIS-specific noise phenomena at the required energies. However, an X-ray optimized variant, the CIS221-X, shows more promising performance in this first test of its soft X-ray detection capability. Modelling and initial experiments suggest that the CIS221-X meets and exceeds the energy resolution requirements of AXIS, though follow up tests with BSI sensors to test sub-1 keV sensitivity and after irradiation to evaluate likely in-flight performance will greatly improve understanding of this X-ray detector.

Of the alternatives considered, the CCD311 and CIS221-X are viable X-ray detectors for this application. Though both X-ray detectors currently have low TRL, their development and testing is tied to other instrument development programs and their use could be de-risked if mission timelines align favorably.

5. ACKNOWLEDGEMENTS

This presentation has been supported by a Royal Astronomical Society conference travel grant.

REFERENCES

[1] Narendranath, S., private communication, "AXIS Baseline Design document," Space Astronomy Group, ISRO.
[2] Harding, L. K., Demers, R. T., Hoenk, M., Peddada, P., Nemati, B., Cherng, M., Michaels, D., Neat, L. S., Loc, A., Bush, N., Hall, D., Murray, N., Gow, J., Burgon, R., Holland, A., Reinheimer, A., Jorden, P. R. and Jordan, D., "Technology advancement of the CCD201-20 EMCCD for the WFIRST coronagraph instrument: sensor characterization and radiation damage," J. Astron. Telesc. Instruments, Syst. **2**(1), 011007 (2015).
[3] Bush, N., Heymes, J., Hall, D., Holland, A. and Jordan, D., "Measurement and optimization of clock-induced charge in electron multiplying charge-coupled devices," J. Astron. Telesc. Instruments, Syst. **7**(01), 1–24 (2021).
[4] Robbins, M. S. and Hadwen, B. J., "The noise performance of electron multiplying charge-coupled devices," IEEE Trans. Electron Devices **50**(5), 1227–1232 (2003).
[5] Teledyne e2v., "CIS120 Datasheet," 1 (2017).
[6] Soman, M. R., Allanwood, E. A. H., Holland, A. D., Stefanov, K., Pratlong, J., Leese, M., Gow, J. P. D. and Smith, D. R., "Electro-optic and radiation damage performance of the CIS115, an imaging sensor for the JANUS optical camera onboard JUICE," High Energy, Opt. Infrared Detect. Astron. VII **9915**, 991515 (2016).
[7] Heymes, J., Stefanov, K. D., Soman, M. R., Gorret, D., Hall, D. J., Minoglou, K., Morris, D., Pratlong, J., Prod'homme, T., Tsiolis, G. and Holland, A. D., "Development of a photon-counting near-fano-limited x-ray CMOS image sensor for THESEUS' SXI," X-Ray, Opt. Infrared Detect. Astron. IX(December 2020), A. D. Holland and J. Beletic, Eds., 19, SPIE (2020).
[8] Heymes, J., Ivory, J., Buggey, T., Hetherington, O., Soman, M. and Holland, A., "Characterisation of a soft X-ray optimised CMOS Image Sensor," J. Instrum. **19**(05), P05003 (2022).
[9] Soman, M. R., Hall, D. J., Holland, A. D., Burgon, R., Buggey, T., Skottfelt, J., Sembay, S., Drumm, P., Thornhill, J., Read, A., Sykes, J., Walton, D., Branduardi-Raymont, G., Kennedy, T., Raab, W., Verhoeve, P., Agnolon, D. and Woffinden, C., "The SMILE Soft X-ray Imager (SXI) CCD design and development," J. Instrum. **13**, C01022--C01022 (2018).
[10] Moody, I., Watkins, M., Bell, R., Soman, M., Keelan, J. and Holland, A., "CCD QE in the Soft X-ray Range," 1–16 (2017).
[11] Randall, G., Parsons, S., Hall, D. J., Buggey, T. W., Hetherington, O., Leese, M., Holland, A. D., Yeoman, D. and Soman, M. R., "Processing x-ray data on board the SMILE SXI," X-Ray, Opt. Infrared Detect. Astron. IX(December), A. D. Holland and J. Beletic, Eds., 30, SPIE (2020).
[12] Tutt, J. H., Holland, A. D., Hall, D. J., Harriss, R. D. and Murray, N. J., "The noise performance of electron-multiplying charge-coupled devices at X-ray energies," IEEE Trans. Electron Devices **59**(1), 167–175 (2012).